

New $H(z)$ measurement at Redshift = 0.12 with DESI Data Release 1

ZE-FAN WANG(王泽凡) ^{1,2} LEI LEI(雷磊) ^{1,2} AND YI-ZHONG FAN(范一中) ^{1,2}

¹*Key Laboratory of Dark Matter and Space Astronomy, Purple Mountain Observatory, Chinese Academy of Sciences, Nanjing 210023, China*

²*School of Astronomy and Space Science, University of Science and Technology of China, Hefei 230026, China*

ABSTRACT

The Hubble parameter ($H(z)$) is a function of the redshift and a reliable measurement is very important to understand the expansion history of the Universe. In this work, we perform full-spectrum fitting using BAGPIPES on more than four thousand massive, passively evolving galaxies released by the DESI collaboration to estimate their cosmological-independent stellar ages and star-formation histories, and derive a new measurement of $H(z = 0.12) = 71.33 \pm 4.20 \text{ km s}^{-1} \text{ Mpc}^{-1}$, which is well consistent with those derived in other ways.

Keywords: Galaxies (573) — Observational Cosmology (1146) — Hubble constant (758)

1. INTRODUCTION

Modern cosmology is built upon the Λ CDM framework, which features a cosmological constant (Λ) and cold dark matter (CDM). The cosmological constant Λ drives the accelerated expansion of the Universe, while CDM plays a central role in the formation of galaxies and large-scale structure. This paradigm has been firmly established through multiple cosmological probes, including the cosmic microwave background (CMB; G. F. Smoot et al. 1992; Planck Collaboration et al. 2020), Type Ia supernovae (A. G. Riess et al. 1998; D. Brout et al. 2022), and baryon acoustic oscillations (BAO; W. J. Percival et al. 2001; D. J. Eisenstein et al. 2005; M. Abdul Karim et al. 2025). Within this model, the Hubble constant is a fundamental observable, directly related to the present expansion rate of the Universe and its inferred age. However, the increasing precision of these measurements has revealed a significant tension in the inferred value of this parameter (E. Abdalla et al. 2022; M. Kamionkowski & A. G. Riess 2023). It is therefore crucial to develop and employ independent probes (M. Moresco et al. 2022) to determine whether this discrepancy arises from unresolved systematic effects or signals new physics beyond the standard cosmological model (E. Di Valentino et al. 2021).

Under the assumption of a Friedmann–Lemaître–Robertson–Walker (FLRW) metric, the Hubble parameter can be expressed as a function of redshift,

$$H(z) = -\frac{1}{1+z} \frac{dz}{dt}, \quad (1)$$

where z denotes redshift and t is the cosmic time. A straightforward approach to addressing the Hubble tension is to extrapolate $H(z)$ to zero redshift. Accordingly, two main methods have been proposed to measure the expansion history of the Universe: one based on the radial BAO scale (D. Eisenstein 2003; C. Blake & K. Glazebrook 2003), and the other relying on the differential galaxies’ age method (R. Jimenez & A. Loeb 2002). The former exploits the inverse relationship between $H(z)$ and the differential radial comoving distance, which can be inferred from the radial extent of BAO features across redshift. However, this technique requires a prior calibration of the comoving BAO scale, typically derived from CMB observations. As a result, BAO-based measurements are not strictly cosmological model-independent, since the sound horizon scale is usually inferred within a specific cosmological framework (Planck Collaboration et al. 2020).

The second approach determines the Hubble parameter by measuring the differential age–redshift relation of galaxies. In this case, $H(z)$ is directly calculated from the local derivative of cosmic age (dt) with respect to redshift (dz), and systematic offsets associated with absolute age measurements are largely mitigated. Therefore, the careful selection of a class of galaxies that can serve as reliable “clocks” is crucial for this method. R. Jimenez & A. Loeb (2002) proposed that massive and passively evolving galaxies are optimal candidates for such “cosmic chronometers” (CCs). Numerous studies have shown that these galaxies formed the bulk of their stellar mass rapidly and at high redshift (L. L. Cowie et al. 1996; M. Moresco et al. 2011; A. Gallazzi et al. 2014; A. C. Carnall et al. 2019, 2022), resulting in a homogeneous and synchronized stellar population that effectively acts as a cosmic chronometer (L. L. Cowie et al. 1996; D. Thomas et al. 2010; A. C. Carnall et al. 2018). Alternatively, the age of quasars with higher redshifts can also be used to calculate the lower limit of $H(z)$ (S. Vagnozzi et al. 2022). To construct a pure CC sample, a variety of selection criteria have been employed, including galaxy morphology (E. P. Hubble 1982), color–color cuts (O. Ilbert et al. 2013; M. Moresco et al. 2012, 2016), spectral energy distribution (SED) fitting (L. Pozzetti et al. 2010), and spectroscopic features such as Lick indices (M. Moresco et al. 2018; N. Borghi et al. 2022b). Comparisons among different selection strategies indicate that a relatively mature and robust procedure for constructing CC samples has been established (M. Moresco et al. 2013, 2018, 2022).

Determining accurate galaxy ages, however, remains challenging. A number of approaches have been explored, including full-spectrum fitting (J. Simon et al. 2005; C. Zhang et al. 2014; E. Tomasetti et al. 2023; K. Jiao et al. 2023) and methods based on specific spectral regions or indices (M. Moresco et al. 2012, 2016; N. Borghi et al. 2022a). As a largely model-independent probe, CC-based measurements of $H(z)$ provide a robust dataset for testing cosmological models and constraining the properties of dark energy (L. A. Escamilla et al. 2023; L. Lei et al. 2026; Y.-Y. Wang et al. 2026).

In this work, we make use of Data Release 1 (DR1) from the Dark Energy Spectroscopic Instrument (DESI), together with the DESI Legacy Imaging Surveys, which provide an extensive repository of high-quality spectroscopic and photometric data. We perform full-spectrum fitting using BAGPIPES³ (A. C. Carnall et al. 2018) on more than four thousand massive, passively evolving galaxies to estimate their stellar ages and star-formation histories, and derive a new measurement of $H(z)$ at low redshift. This paper is organized as follows. In Section 2, we describe the data and sample selection. In Section 3, we present the methodology and details of the full-spectrum fitting procedure.

³ Bayesian Analysis of Galaxies for Physical Inference and Parameter ESTimation (BAGPIPES): <https://bagpipes.readthedocs.io>

In Section 4 we show our properties of selected sample and discuss the $H(z)$ measurements. The last section concludes the whole paper.

2. DATA

2.1. *DESI Survey*

DESI is a powerful spectrometric facility mounted on the Nicholas U. Mayall 4-meter Telescope at Kitt Peak National Observatory in Arizona ([DESI Collaboration et al. 2022](#); [E. F. Schlafly et al. 2023](#); [J. Guy et al. 2023](#)). DESI employs 5,000 robotic fiber positioners over a 3.2-degree field of view, enabling the simultaneous acquisition of thousands of spectra. The instrument provides continuous wavelength coverage from 3600 to 9800 Å with a spectral resolution of $R \sim 2000 - 5000$ ([C. Poppett et al. 2024](#); [J. H. Silber et al. 2023](#); [T. N. Miller et al. 2024](#)). DESI DR1 marks a monumental milestone for the project, serving as the first major public release of data from the Main Survey operations ([DESI Collaboration et al. 2025](#)). Covering observations taken between May 2021 and June 2022, DR1 presents a large catalog of extragalactic spectroscopy. The release contains high-quality spectra for over 18 million unique targets, including approximately 13 million galaxies and 1.6 million quasars, alongside roughly 4 million stars from our own Milky Way.

DESI spectroscopic targets are selected primarily from the DESI Legacy Imaging Surveys, which provide uniform optical (g , r , z) photometry over $\sim 20,000$ deg², complemented by mid-infrared data ($W1$, $W2$, $W3$ and $W4$) from Wide-field Infrared Survey Explorer ([H. Zou et al. 2017](#); [A. Dey et al. 2019](#)). The Legacy Surveys are approximately two magnitudes deeper than Sloan Digital Sky Survey and form the photometric foundation for DESI target selection, ensuring a well-defined and homogeneous parent sample for statistical analyses.

As our work intends to do, the galaxy sample can be used to measure the precise value of $H(z)$. All data and Value-Added Catalogs (VACs)⁴ used in this work are now publicly available. We retrieve the data from SPectra Analysis and Retrievable Catalog Lab (SPARCL) and the Astro Data Lab ([M. J. Fitzpatrick et al. 2014](#); [R. Nikutta et al. 2020](#)). There is **an** issue⁵ in flux uncertainty estimation of DESI DR1 data and we use a step function to fix this.

2.2. *Sample Selection*

In this study, we utilize the Stellar Mass and Emission Line Catalog ([H. Zou et al. \(2024\)](#) and [Zou Hu et al. \(2025\)](#) in preparation). This catalog provides the stellar mass and emission line measurements for all galaxies in DESI DR1 with reliable redshift measurements. Stellar mass is derived by using CIGALE ([S. Noll et al. 2009](#); [P. Serra et al. 2011](#)), which employs the broad-band g , r , z , $W1$, and $W2$ photometry from the DESI Legacy Imaging Surveys, and spectrophotometry of 10 artificial bands generated through convolution with DESI spectra. Main optical emission lines are measured by a single Gaussian fit, with absorption correction through continuum fitting performed by STARLIGHT ([R. Cid Fernandes et al. 2005, 2007](#)). Additionally, the catalog includes stellar population properties derived by CIGALE and those obtained by STARLIGHT using DESI spectra.

Particularly, we perform the sample selection by following steps:

1. **Galaxy morphology selection:** The catalog provides the morphological type of galaxies and we specially select the early-type galaxies, namely `MORPHTYPE == DEV` in the catalog.

⁴ <https://data.desi.lbl.gov/doc/releases/dr1>

⁵ <https://data.desi.lbl.gov/doc/releases/dr1/known-issues/>

2. **Mass and specific star formation rate (sSFR) cut:** Next, we select stellar mass $\log_{10}(M_*/M_\odot) > 11$ and constrain the sSFR ($\text{sSFR} = \text{Star Formation Rate}/M_*$), $\log_{10}(\text{sSFR}) < -11$ to select quiescent galaxies.
3. **Emission line cut:** We clean the sample with obvious emission lines. We choose the equivalent width (EW) of [O II], [H β], [H α] $< 4 \text{ \AA}$ and the signal-to-noise ratio (S/N) of these emission line < 3 .
4. **H/K cut:** Another diagnostic is the ratio of two absorption lines, CaII H at 3969 \AA and CaII K at 3934 \AA . We measure two pseudo-Lick indices with `pyLick`⁶ (N. Borghi et al. 2022b) and select the galaxies with $H/K < 1.3$.
5. **Redshift cut:** In order to fully use the DESI spectra and select high S/N sample, we decide to cut the redshift of our sample $z < 0.2$ and the key word `FLUX SCALE` in the catalog > 3 .

3. METHOD

We utilize a modified version of the public code `BAGPIPES` whose cosmological prior is removed (detailed modification in sec.3 of K. Jiao et al. (2023)) to fit jointly spectra and photometry with a Bayesian approach (A. C. Carnall et al. 2019).

3.1. Basics of BAGPIPES

`BAGPIPES` models observed spectra and photometry by forward-modeling synthetic observables over a parameter space and inferring posterior distributions through Bayesian inference. The exploration of the parameter space and the estimation of posterior probabilities are performed using a nested sampling algorithm, either `MultiNest`⁷ (F. Feroz et al. 2019; J. Buchner et al. 2014) or `Nautilus`⁸ (J. U. Lange 2023), which efficiently samples high-dimensional and potentially degenerate parameter spaces. In this research, we use the `Nautilus` sampling algorithm and its default setting by `BAGPIPES`

The physical model implemented in `BAGPIPES` consists of these main components:

- Stellar population synthesis (SPS). The intrinsic stellar emission is modeled using the 2016 version of the G. Bruzual & S. Charlot (2003) stellar population synthesis models, constructed assuming a P. Kroupa (2001) initial mass function.
- Star formation history (SFH). The star formation history, $\text{SFR}(t)$, describes the temporal build-up of stellar mass and sets the relative contribution of SSPs of different ages. `BAGPIPES` allows for flexible parametric forms of SFH, enabling both rapid early formation and extended star formation scenarios. The specific forms adopted in this work are described in Section 3.1.1.
- Interstellar medium (ISM) transmission. For the ionized phase, we follow the prescriptions of S. Charlot & M. Longhetti (2001) to account for nebular emission and continuum associated with recent star formation. This optional component is included to conservatively capture potential residual ionized gas contributions. Regarding the neutral ISM, dust attenuation is implemented via wavelength-dependent transmission functions that modify the intrinsic stellar spectrum, allowing for the adoption of various attenuation laws.

⁶ `pyLick`: <https://pylick.readthedocs.io/>

⁷ <https://johannesbuchner.github.io/PyMultiNest/>

⁸ <https://nautilus-sampler.readthedocs.io/en/stable/>

In addition to these physical components, BAGPIPES provides optional non-physical modules to account for residual calibration mismatches between spectra and photometry, as well as additional noise terms to correct for underestimated observational uncertainties. These settings and their implementation are described in detail in Section 3.2.

3.1.1. SFH choice

The traditional approach to SED fitting has been to use a simple functional form to parameterize the SFH. In this work, we choose 2 commonly used forms to reconstruct the SFHs of CC:

1. The delayed exponentially declining (DED) SFH, which can be expressed as

$$\text{SFR}(t) \propto \begin{cases} (t - T_0)e^{-\frac{t-T_0}{\tau}} & t \geq T_0 \\ 0 & t < T_0 \end{cases}, \quad (2)$$

where T_0 represents the time when star formation begins and τ is the timescale after which SFR declines exponentially. It is a typical form for quiescent galaxy because it is characterized by a burst episode of star formation followed by passive evolution (A. Citro et al. 2017).

2. The double-power-law (DPL) SFH, which can be expressed as

$$\text{SFR}(t) \propto \left[\left(\frac{t}{\tau} \right)^\alpha + \left(\frac{t}{\tau} \right)^{-\beta} \right]^{-1}, \quad (3)$$

where α and β are the falling and rising slopes respectively, and τ is also related to the time at which star formation peaks. It is worthwhile to note that E. Tomasetti et al. (2023) found the decoupling between the rising and falling slopes may lead to non-physical SFHs. To address this, we impose a conservative prior on β in the range 10 to 1000, and assign α a logarithmic prior between 0.1 and 1000. The parameter τ is allowed to vary between 0 and 20 in a uniform prior.

It is clear that there is a beginning of star formation in Equation 2. The definition of galaxies' age can be directly written as

$$\text{age} = t_U(z_{obs}) - T_0, \quad (4)$$

where $t_U(z_{obs})$ is the age of the universe at the redshift of observation. On the other hand, Equation 3 has no obvious beginning nor the end of star formation. Hence, BAGPIPES offer an alternative age named *mass-weighted age*, which is expressed as

$$\text{age}_{mw} = t_U(z_{obs}) - \frac{\int_0^{t_{obs}} t \text{SFR}(t) dt}{\int_0^{t_{obs}} \text{SFR}(t) dt}. \quad (5)$$

The *mass-weighted age* provides a robust estimate of the typical stellar age in a galaxy, as T_0 is modified by averaging the SFR(t) of galaxy, giving higher importance to those that contribute most to the total stellar mass. Thus, it primarily represents the time when the main bulk of star formation occurred. When using the Equation 3 as SFH parameterization, the galaxy age provided by BAGPIPES is the *mass-weighted age*.

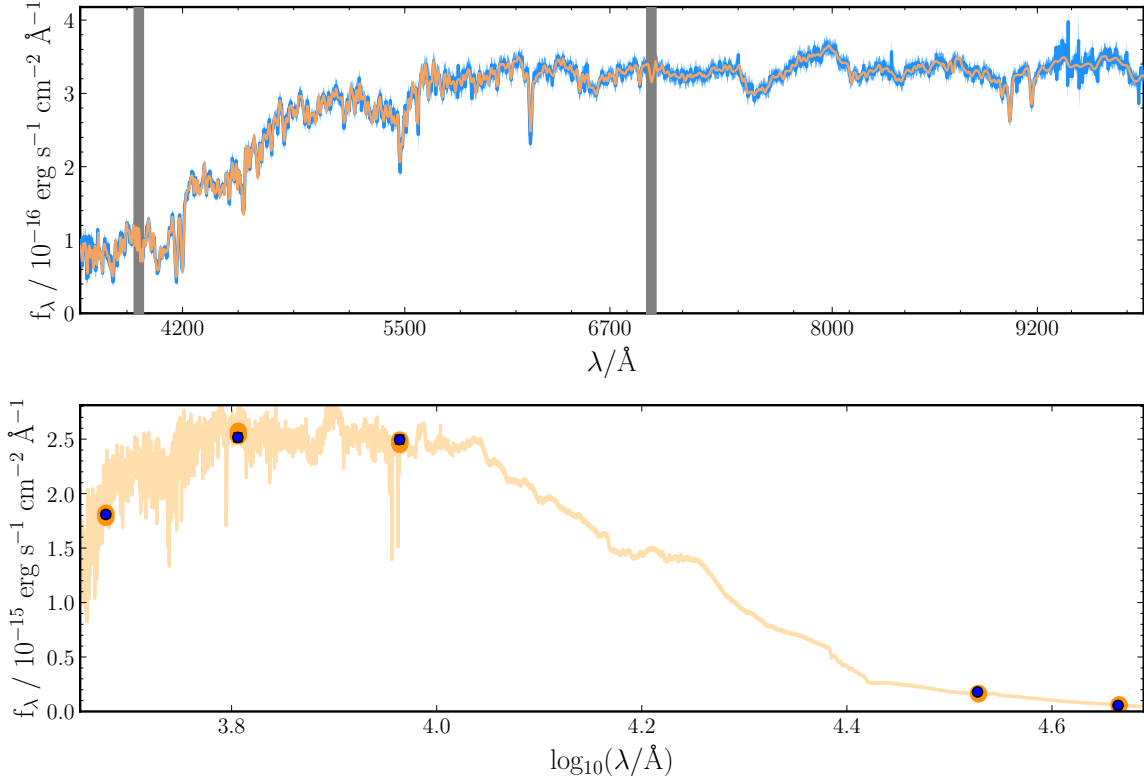


Figure 1. A typical CC (TARGETID = 2851244993413120) fitting result. Spectrum and photometry observation data are shown in blue, best-fit results are shown in orange. Gray areas are masked when fitting.

3.2. fitting with DESI spectra

Before fitting the data, we check the potential anomalies in observation, finding an issue similar to E. Tomasetti et al. (2023). The S/N of the photometry is far larger than that of spectrum. To fix this circumstance, we assume the S/N for the photometry to be twice larger than the S/N of each spectrum⁹. In this way, we balance these two observations and also, the DESI DR1 spectra were binned by a factor of four to speed up the fitting as well as reduce the noise.

We tested two fitting configurations whose major difference is the choices of SFH. The left identical components are listed below:

- a dust component described by D. Calzetti et al. (2000). Regarding the stellar continuum attenuation, we impose a uniform prior on the V -band optical depth within the range $0 < A_V < 8$. The attenuation factor is fixed at $\epsilon = 2$, representing the ratio of dust attenuation in stellar birth clouds relative to the diffuse ISM. Additionally, we set the lifetime of these birth clouds to $t_{BC} = 10$ Myr; consequently, emission from stars formed within the last 10 Myr is subject to twice the attenuation experienced by the older population;
- a nebular emission component described by A. C. Carnall et al. (2018) using the CLOUDY (G. J. Ferland et al. 2017). Our sample selection should have already excluded this type of objects, but we include it in the model due to a more realistic physical simulation as well as an additional

⁹ In this context, the S/N of a spectrum is defined as the median of the whole spectrum.

check of its absence. We fix the ionization parameter to $\log_{10}(U) = -3$ and mask the rest-frame region from 3702–3752 Å, 6535–6585 Å due to the ambiguities of low-level emission in quiescent galaxies. These two areas contain the [O II] and [H α] emission line. AGN and ionization from old stars both thought to contribute to this phenomenon (R. Singh et al. 2013; F. Herpich et al. 2018).

- a Gaussian process noise model described in A. C. Carnall et al. (2019). Normally, the flux uncertainty of spectra is treated as uncorrelated or white noise. However, this hypothesis does not work when facing consecutive spectra pixels, due to many data-reduction steps from the raw spectroscopic observations into 1D spectral arrays (B. Panter et al. 2003; S. Belli et al. 2019). Thus, a noise model based on Gaussian process is proposed, which used a covariance matrix describing the covariance between two wavelength bins:

$$C_{jk}(\Phi) = a^2 \sigma_j \sigma_k \delta_{jk} + b^2 \exp\left(-\frac{(\lambda_j - \lambda_k)^2}{2l^2}\right) \quad (6)$$

where $C_{jk}(\Phi)$ is the covariance matrix, Φ is the nuisance parameters, $\sigma_{j,k}$ are the uncertainties on our pixel fluxes, $\lambda_{j,k}$ are the central wavelengths of our pixels, $\delta_{j,k}$ is the Kronecker delta function, and a, b and l are free parameters. The first term of Equation 6 deals with the uncorrelated noise and the second term represents the correlation between pixels. Appendix B shows a more detailed for this model.

- a second-order Chebyshev polynomial calibration component (A. C. Carnall et al. 2019). This is designed for potential flux loss owing to a bunch of issues like the aperture correction and mismatching between the models and data. We apply Gaussian priors to the first and second polynomial coefficients with standard deviations of $\sigma = 0.25$. The prior means are $\mu = 0$ for the first and second order. For the zero order, we apply an uniform prior from 2 to 50 according to the FLUX SCALE in the DESI catalog for aperture correction.

The parameter space and prior form are concluded in Table 1.

We assess the convergence of the results and employ Hartigan & Hartigan’s dip test to evaluate the unimodality (single peak) of the posterior distributions (J. A. Hartigan & P. M. Hartigan 1985; P. Hartigan 1985). The dip test, with the null hypothesis that the distribution is unimodal, measures multimodality by computing the maximum difference, across all sample points, between the empirical distribution function and the unimodal distribution function that minimizes this maximum difference. A p-value threshold of 0.05 for the physical properties (age, τ , formed mass, metallicity, redshift, stellar velocity dispersion (σ_{vel})) is adopted to ensure unimodality of the posterior distributions. To assess whether a posterior is significantly skewed towards the parameter space boundary, we calculate the adjusted Fisher-Pearson standardized moment coefficient of the posterior distributions. We impose a requirement that the skewness of the redshift and σ_{vel} posterior distributions be less than one, while the skewness of the remaining parameters must be below 1.5. If these requirements are not met, the results can not be considered valid, and are discarded as bad fit. A typical good fitting result is shown in Figure 1 and its associated corner plot in Figure 10. Two inferred SFHs are illustrated in Figure 2.

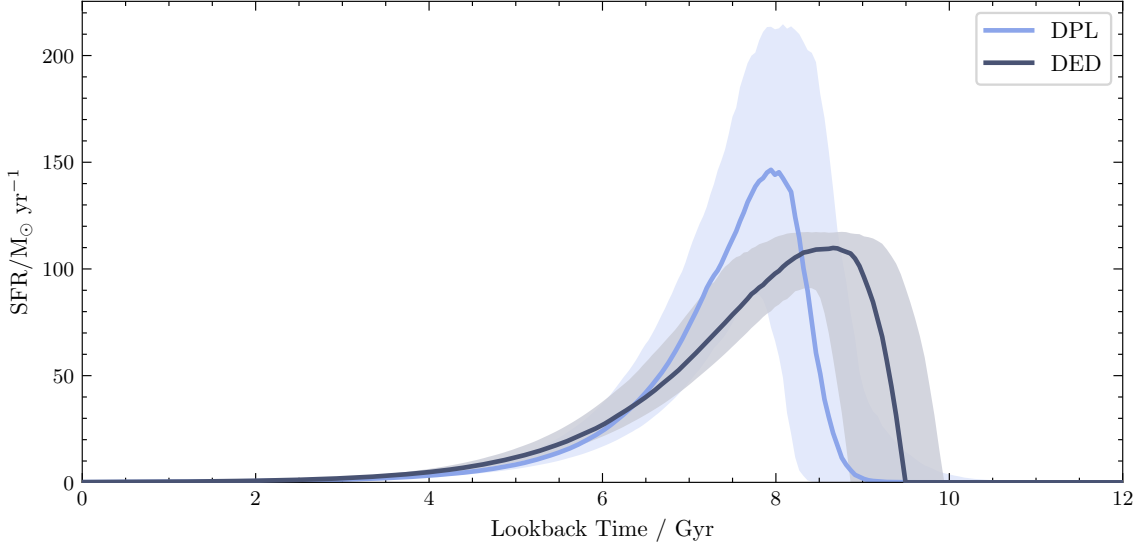


Figure 2. Comparison of the TARGETID = 2851244993413120’s reconstructed star formation history profiles between the DED (dark blue) and DPL (light blue) models. The horizontal axis represents the lookback time in Gyr, and the vertical axis shows the star formation rate (SFR) in $M_{\odot} \text{ yr}^{-1}$. In both cases, the solid lines indicate the median of the posterior distribution, while the shaded regions represent the 1σ uncertainties.

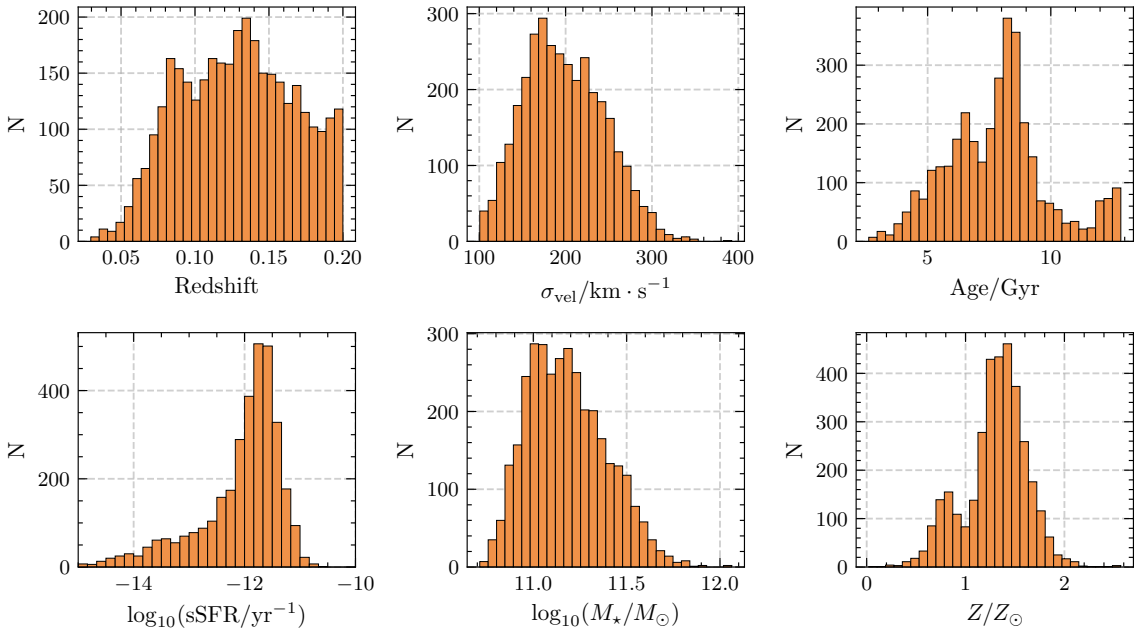


Figure 3. Distributions of the inferred physical properties for our CC sample, derived from BAGPIPES. The panels show the distribution of posterior median values for the spectroscopic redshift, stellar velocity dispersion (σ_{vel}), stellar age, sSFR ($\log_{10}(\text{sSFR}/\text{yr}^{-1})$), stellar mass ($\log_{10}(M_{\star}/M_{\odot})$) and metallicity relative to solar (Z/Z_{\odot}), respectively.

Table 1. Parameters and priors for the model we fit to our data. For Gaussian priors, μ is the mean and σ the standard deviation of the prior distribution. Logarithmic priors are uniform in log base ten of the parameter. z_{spec} is the redshift obtained from the catalog. For the metallicity prior, numerous literature illustrated that CCs have slightly super-solar metallicity (M. Onodera et al. 2012; C. Conroy et al. 2014; M. Kriek et al. 2019; M. Moresco et al. 2022). Thus, we impose an 1.3 in mean and a wide $\sigma = 0.8$.

Component	Parameter	Symbol / Unit	Range or Values	Prior	Hyperparameters
Global	Redshift	z	$z_{spec} \pm 3\sigma$	Gaussian	$\mu = z_{spec}, \sigma = 0.01$
	Velocity dispersion	$\sigma_{vel} / \text{km s}^{-1}$	(10, 400)	logarithmic	
	Ionization parameter		$\log_{10}(U) = -3$		
SFH	Formed stellar mass	M_{formed} / M_{\odot}	(1, 10^{13})	logarithmic	
	Metallicity	Z / Z_{\odot}	(0, 3)	Gaussian	$\mu = 1.3, \sigma = 0.8$
DED	Age	Age / Gyr	(0.1, 20)	logarithmic	
	Star formation timescale	τ / Gyr	(0, 1)	uniform	
DPL	Falling slope	α	(0.1, 1000)	logarithmic	
	Rising slope	β	(10, 1000)	logarithmic	
	Peak time	τ / Gyr	(0, 20)	uniform	
Dust	Attenuation at 5500Å	A_V / mag	(0, 8)	uniform	
	Attenuation factor	ϵ	2		
	Lifetime of stellar birth clouds	t_{BC} / Gyr	0.01		
Calibration	Zero order	P_0	(2, 50)	uniform	
	First order	P_1	(-0.5, 0.5)	Gaussian	$\mu = 0, \sigma = 0.25$
	Second order	P_2	(-0.5, 0.5)	Gaussian	$\mu = 0, \sigma = 0.25$
Noise	White noise scaling	a	(0.1, 10)	logarithmic	
	Correlated noise amplitude	b / f_{max}	(0.0001, 1)	logarithmic	
	Correlation length	$l / \Delta\lambda$	(0.006, 1)	logarithmic	

4. RESULT

4.1. Galaxy properties

Following the full-spectrum fitting procedure, we impose a stringent mass and σ_{vel} threshold of $\log_{10}(M_{formed}/M_{\odot}) > 11$ and $\sigma_{vel} > 100$ km/s to ensure the homogeneity of our CC sample, which results in 3429 CCs in total¹⁰. The distributions of the main physical parameters (redshift, σ_{vel} , age, sSFR, stellar mass, metallicity) are illustrated in Figure 3. Four parameters (age, τ , metallicity and stellar mass) are illustrated in Figure 4 as a function of redshift. Each galaxy is color-coded by its median σ_{vel} . Unless otherwise specified, we report the physical properties using the median values along with the 16th and 84th percentiles. Overall, our CC sample is characterized by:

- High stellar masses: $\log_{10}(M_{\star}/M_{\odot}) = 11.16^{+0.25}_{-0.19}$;

¹⁰ Note that formed stellar mass (M_{formed}) is not the same as living stellar mass (M_{\star}) in BAGPIPES. M_{formed} is defined as $M_{formed} = \int_0^t \text{SFR}(t') dt'$, which represents the whole stellar mass formed from $t = 0$ to the time t . M_{\star} on the other hand excludes remnants.

- Low dust attenuation and sSFR: $A_V = 0.10_{-0.07}^{+0.13}$ mag and sSFR is $\log_{10}(\text{sSFR}/\text{yr}^{-1}) < -10$, which are typical for massive and passive galaxies;
- Rapid SFH: $\tau = 0.76_{-0.23}^{+0.15}$ Gyr;
- Super-solar metallicities: $Z/Z_{\odot} = 1.33_{-0.44}^{+0.24}$, we can clearly see a double peak on the metallicity distribution. The majority of our sample is slightly above solar, while there is a tiny peak below the solar metallicity. This secondary, metal-poor peak likely originates from the dust–metallicity degeneracy in fitting (K. Jiao et al. 2023) or may suggest the presence of a sub-population within our CC sample which has slightly sub-solar metallicity (M. Kriek et al. 2019; A. C. Carnall et al. 2022), likely reflecting different chemical enrichment histories.

Remarkably, even without invoking a cosmological prior, the derived stellar ages for the majority of our sample exhibit a declining trend with redshift that is consistent with the Λ CDM model (Planck Collaboration et al. 2020). We identify a clear positive correlation between stellar mass and σ_{vel} . Regarding the SFH timescale τ , we find no significant evolution with redshift; however, our sample recovers the “mass-downsizing” scenario, where more massive galaxies characterize shorter formation timescales (L. L. Cowie et al. 1996; D. Thomas et al. 2010; A. Citro et al. 2017). Besides, the lack of significant redshift dependence in metallicity and mass further validates our selection criteria in isolating a synchronized population of CCs.

In summary, we have constructed a robust and representative CC sample. In the following section, we will discuss the computation of $H(z)$.

4.2. Computing $H(z)$ measurement

To derive $H(z)$ from Equation 1, first, we need to construct the median age–redshift relation using the selected CC sample. The sample is partitioned into both redshift and stellar mass intervals. Within each sub-sample, we determine the median age and the corresponding mean redshift. The uncertainty associated with the age is estimated as MAD/\sqrt{n} , where MAD denotes the median absolute deviation and n is the number of galaxies per bin. To mitigate progenitor bias (M. Franx 1995; P. G. van Dokkum et al. 2000), we divide the sample into two mass bins according to the median value, $\log_{10}(M_{\star}/M_{\odot}) = 11.16$. Here we choose to split the redshift into four equally spaced intervals and we consider this scheme as the benchmark for our research. The age–redshift relation for the benchmark case is presented in Figure 5 and the values are reported in Table 2.

The next step is to individually calculate the $H(z)$ points on every mass bin. When estimating the redshift–age derivative ($\frac{dz}{dt}$), we adopt a non-adjacent differencing approach to minimize potential covariance rather than using consecutive bins. Specifically, for a total of N redshift bins within a given mass range, we compute the difference between the i^{th} and the $(i + N/2)^{\text{th}}$ data points. This strategy necessitates an even number of redshift bins, ensuring that each data point is utilized uniquely to avoid spurious correlations between the derived $H(z)$ values (K. Jiao et al. 2023).

Finally, these values are inverse variance averaged to get a single and more accurate estimate of $H(z)$ (M. Moresco et al. 2016; N. Borghi et al. 2022a; E. Tomasetti et al. 2023; K. Jiao et al. 2023). In this way, our $H(z)$ estimation of our benchmark binning is

$$H(z = 0.12) = 71.33 \pm 3.45(\text{stat.}) \text{ km/s/Mpc.}$$

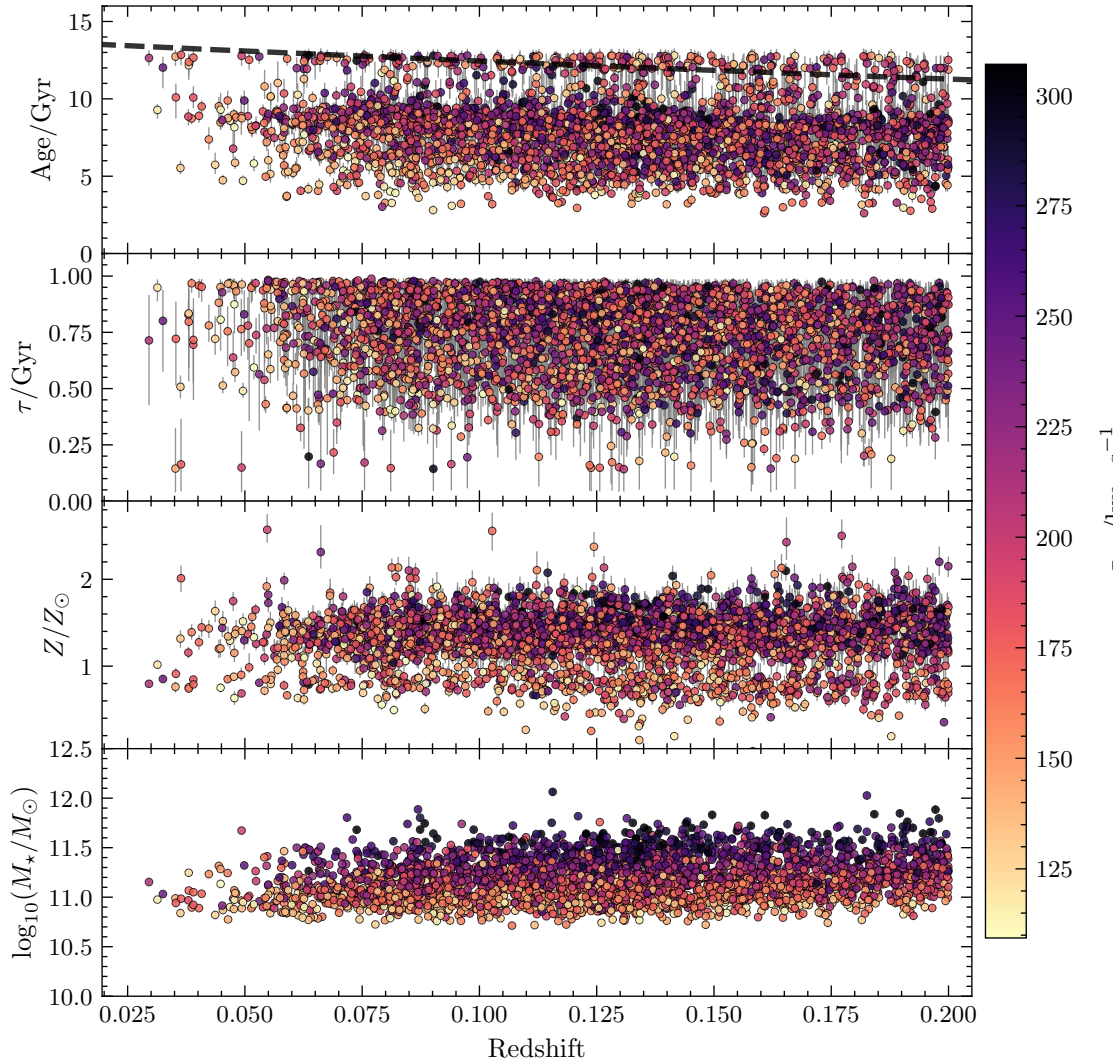


Figure 4. Redshift distribution of stellar age, star formation timescale (τ), metallicity and logarithmic stellar mass ($\log_{10}(M_*/M_\odot)$) obtained from the full-spectrum fitting of our CC sample. Each galaxy is color-coded by its velocity dispersion (σ_{vel}). The black dashed line in the first panel is the age–redshift relation predicted by the [Planck Collaboration et al. \(2020\)](#) Λ CDM model.

The associated error is only statistical and is rather low due to our large CC sample size. In the next section, different binning strategies and SFHs are compared in order to access the systematic effect on our $H(z)$ measurement.

4.3. Discussion on systematic effects

The major sources of systematic uncertainty are binning method, SFH choice and the SPS model ([M. Moresco et al. 2022](#); [E. Tomasetti et al. 2023](#); [K. Jiao et al. 2023](#)). In this research, we did not consider the SPS model effect. We evaluate the impact of different binning configurations by testing four distinct strategies:

- Binning type: either equally spaced (fixed) or equally populated (quant.);
- Binning size: choosing four intervals or two intervals of redshift.

Table 2. Median ages and properties of the selected CC sample considering the benchmark binning. Mean values of redshift, median ages and the number of galaxies in each bin (n) are reported.

	Redshift	Age/Gyr	n
low-mass	0.06	8.33 ± 0.08	178
	0.09	7.73 ± 0.05	590
	0.14	7.33 ± 0.05	617
	0.17	6.62 ± 0.07	330
high-mass	0.07	8.87 ± 0.07	106
	0.1	8.54 ± 0.04	479
	0.18	7.95 ± 0.05	514

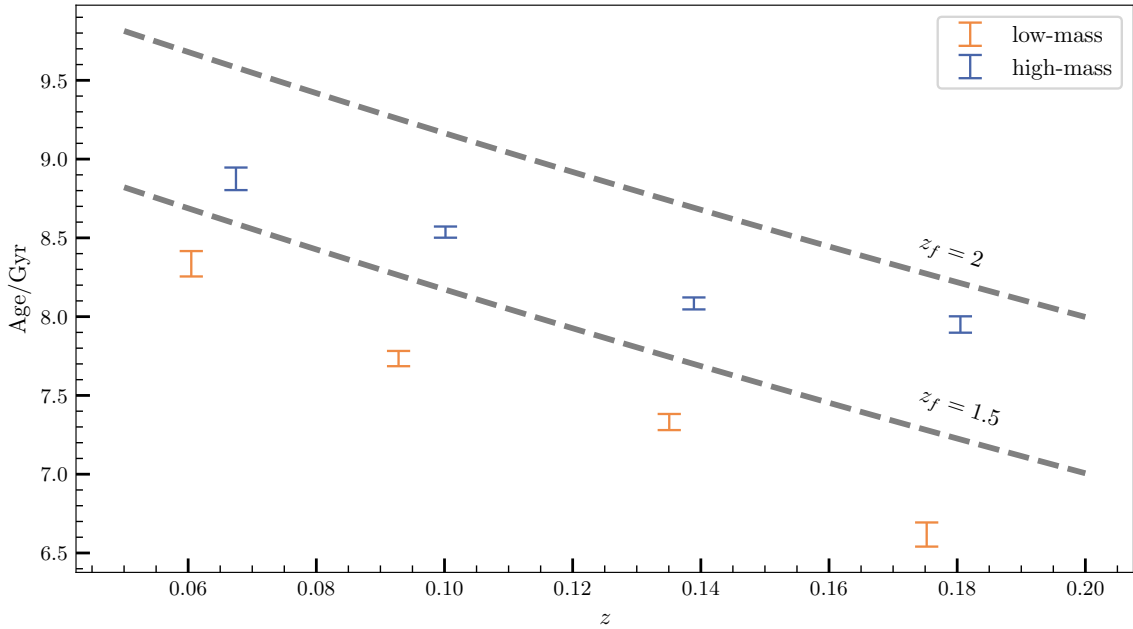


Figure 5. Median-binned age–redshift relations for our baseline results. The blue and orange points represent the lower and higher mass bins divided by the median value. For illustration, we also present the redshift z_f of galaxy formation (gray dashed lines) within the Λ CDM model by [Planck Collaboration et al. \(2020\)](#).

The configuration utilizing equally spaced and dividing into four bins is designated as the benchmark, while the remaining three strategies serve as comparative cases to assess systematic effects. Other

Table 3. Measurements of $H(z)$ obtained applying the CC method with different binning and SFH configurations.

SFH	Binning	z	$H(z)/\text{km} \cdot \text{s}^{-1}\text{Mpc}^{-1}$
DED	4 fixed	0.12	71.33 ± 3.45
	4 quant.	0.13	70.01 ± 3.86
	2 fixed	0.12	69.42 ± 3.71
	2 quant.	0.13	69.44 ± 4.08
DPL	4 fixed	0.12	73.00 ± 4.16

measurements are shown in Table 3. Furthermore, results with DPL are also listed to assess the SFH contribution of systematics.

The discrepancy in different binning strategies is included as the mean value of difference subtracted by benchmark, $\Delta H_{\text{bin}} = \pm 1.71 \text{ km} \cdot \text{s}^{-1}\text{Mpc}^{-1}$. The SFH contribution to systematic is $\Delta H_{\text{SFH}} = \pm 1.67 \text{ km} \cdot \text{s}^{-1}\text{Mpc}^{-1}$. Further discussion on the SFH effect is shown in the Appendix A.

Finally, summing the errors in quadrature, our measurement at redshift 0.12 is

$$H(z = 0.12) = 71.33 \pm 4.20 \text{ km} \cdot \text{s}^{-1}\text{Mpc}^{-1}$$

This is also shown with other $H(z)$ measurements in Figure 6.

5. CONCLUSION

In this paper, we estimate $H(z)$ at redshift 0.12 with the cosmic chronometers selected from DESI DR1. We derive their physical properties from a joint fitting analysis with spectra and photometry using a modified version of public code BAGPIPES which removed its implemented cosmological prior (A. C. Carnall et al. 2018; K. Jiao et al. 2023). Our main results are summarized as follows.

1. We first select a sample of massive and passively evolving galaxies with the Stellar Mass and Emission Line Catalog combining multiple criteria (galaxy morphology, specific star formation rate, stellar mass, H/K indices, emission line);
2. We then perform a joint fitting with two types of SFHs and find that age of most our sample are decreasing with redshift in agreement with the Λ CDM cosmological model. At fixed redshift, more massive galaxies result older than lower mass ones, confirming the mass-downsizing trend at low redshift.
3. With the robust cosmic chronometer sample, we construct an precise age–redshift relation and obtain a new measurement of $H(z = 0.12) = 71.33 \pm 3.45(\text{stat.}) \text{ km/s/Mpc}$. We also test that our result is consistent with other literature, as well as with the prediction of a Λ CDM model assuming
4. We assess the systematic uncertainty of our measurement by varying the binning strategies and SFH in the fit. We estimate a systematic error of $\Delta H_{\text{sys}} = \pm 1.71(\text{bin}) \pm 1.67(\text{SFH}) \text{ km/s/Mpc}$, mainly dominated by different binning plans.

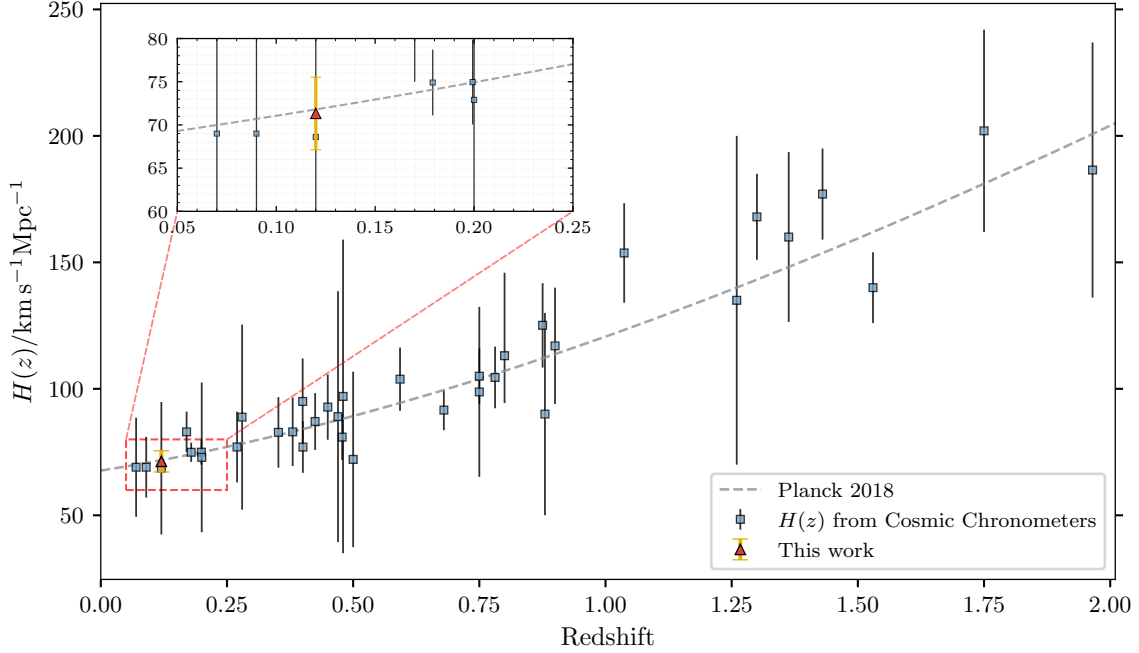


Figure 6. Final $H(z)$ measurement of this work in comparison with all the $H(z)$ estimations obtained up to now with the cosmic chronometer method (J. Simon et al. 2005; D. Stern et al. 2010; C. Zhang et al. 2014; M. Moresco et al. 2012; M. Moresco 2015; M. Moresco et al. 2016; A. L. Ratsimbazafy et al. 2017; N. Borghi et al. 2022a; K. Jiao et al. 2023; E. Tomasetti et al. 2023; R. Jimenez et al. 2023; S. I. Loubser et al. 2025). The gray dashed line represents the $H(z)$ prediction by the Λ CDM model (Planck Collaboration et al. 2020).

5. In the end, we obtain a measurement of the Hubble parameter at redshift 0.12, $H(z = 0.12) = 71.33 \pm 4.20$ km/s/Mpc.

To conclude, this paper consolidate the CC method using full-spectrum fitting technique. Further investigation can be focused on different SPS model (C. Conroy et al. 2009; C. Conroy & J. E. Gunn 2010) and upcoming survey like Euclid (R. Laureijs et al. 2011) and Wide-field Spectroscopic Telescope (R. Bacon et al. 2024; E. Tomasetti et al. 2025) that will significantly improve the census of massive and passive galaxies, especially at $z > 1$.

ACKNOWLEDGMENTS

We thank Dr.Kang Jiao in Zhengzhou University, China and Dr.Adam Carnall in the Institute for Astronomy at Edinburgh University for their useful and constructive feedback to this work. Also, the authors acknowledge [Beijing PARATERA Tech CO.,Ltd.](#) for providing HPC resources that have contributed to our research. This work is supported by the National Natural Science Foundation of China (No.12233011).

This research uses services or data provided by the SPectra Analysis and Retrievable Catalog Lab (SPARCL) and the Astro Data Lab, which are both part of the Community Science and Data Center (CSDC) program at NSF National Optical-Infrared Astronomy Research Laboratory. NOIRLab

is operated by the Association of Universities for Research in Astronomy (AURA), Inc. under a cooperative agreement with the National Science Foundation.

This research used data obtained with the Dark Energy Spectroscopic Instrument (DESI). DESI construction and operations is managed by the Lawrence Berkeley National Laboratory. This material is based upon work supported by the U.S. Department of Energy, Office of Science, Office of High-Energy Physics, under Contract No. DE-AC02-05CH11231, and by the National Energy Research Scientific Computing Center, a DOE Office of Science User Facility under the same contract. Additional support for DESI was provided by the U.S. National Science Foundation (NSF), Division of Astronomical Sciences under Contract No. AST-0950945 to the NSF’s National Optical-Infrared Astronomy Research Laboratory; the Science and Technology Facilities Council of the United Kingdom; the Gordon and Betty Moore Foundation; the Heising-Simons Foundation; the French Alternative Energies and Atomic Energy Commission (CEA); the National Council of Humanities, Science and Technology of Mexico (CONAHCYT); the Ministry of Science and Innovation of Spain (MICINN), and by the DESI Member Institutions: <https://www.desi.lbl.gov/collaborating-institutions/>. The DESI collaboration is honored to be permitted to conduct scientific research on I’oligam Du’ag (Kitt Peak), a mountain with particular significance to the Tohono O’odham Nation. Any opinions, findings, and conclusions or recommendations expressed in this material are those of the author(s) and do not necessarily reflect the views of the U.S. National Science Foundation, the U.S. Department of Energy, or any of the listed funding agencies.

Facility: Astro Data Lab, DESI

Software: SPARCL (Juneau et al. 2024), BAGPIPES (A. C. Carnall et al. 2018), NumPy (C. R. Harris et al. 2020), Astropy (Astropy Collaboration et al. 2013, 2018, 2022), SciPy (P. Virtanen et al. 2020), pandas (Wes McKinney 2010), pyLick (N. Borghi et al. 2022b)

APPENDIX

A. THE DPL SFH RESULTS

Even though we have imposed a conservative prior (See Table 1 and Section 3.1.1) in the DPL SFH configuration, it is still inevitable to arouse the same issue appeared in the E. Tomasetti et al. (2023). In this context, we suppose the major reason is the lack of photometry observations compared to other research (e.g. E. Tomasetti et al. (2023); K. Jiao et al. (2023)). We make comparison of mass-weighted age in two SFH choice in Figure 7 and exclude 3σ outliers to build up our CC sample in DPL measurement.

B. DISCUSSION ON THE NOISE MODEL

During the full-spectrum fitting procedure in section 3.2, we deploy a Gaussian process (GP) noise model. The median of hyperparameter l of our sample is 0.011 and the median of b is 0.014 as shown in the figure 8 below. The major reason we choose this model is that GP model behaves better in red side of the spectrum compared to the white noise (see Figure 1 v.s. Figure 9). However, its substantial computational expense remains a significant drawback. To address this, the latest version of BAGPIPES implements a more efficient algorithm proposed by H.-H. Leung et al. (2024).

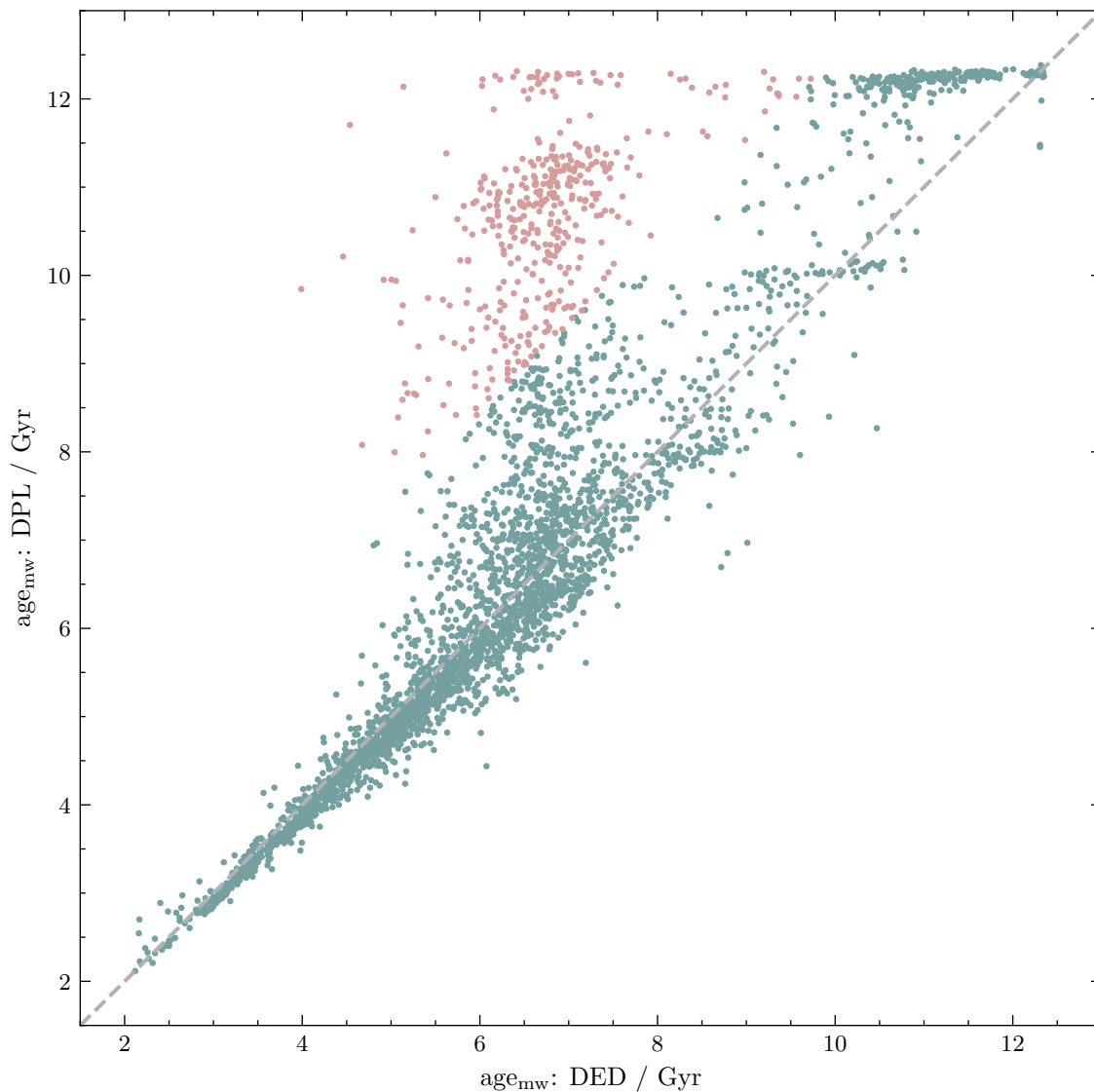


Figure 7. The comparison of mass-weighted ages in two SFHs. The light-red points are excluded as outliers. The gray dashed line is the one-to-one relation.

C. POSTERIOR DISTRIBUTION CORNER PLOT OF A TYPICAL CC

The figure 10 below shows the posterior distribution corner plot of all fitted parameters.

REFERENCES

- Abdalla, E., Abellán, G. F., Aboubrahim, A., et al. 2022, *Journal of High Energy Astrophysics*, 34, 49, doi: [10.1016/j.jheap.2022.04.002](https://doi.org/10.1016/j.jheap.2022.04.002)
- Abdul Karim, M., Aguilar, J., Ahlen, S., et al. 2025, *PhRvD*, 112, 083515, doi: [10.1103/tr6y-kpc6](https://doi.org/10.1103/tr6y-kpc6)
- Astropy Collaboration, Robitaille, T. P., Tollerud, E. J., et al. 2013, *A&A*, 558, A33, doi: [10.1051/0004-6361/201322068](https://doi.org/10.1051/0004-6361/201322068)
- Astropy Collaboration, Price-Whelan, A. M., Sipócz, B. M., et al. 2018, *AJ*, 156, 123, doi: [10.3847/1538-3881/aabc4f](https://doi.org/10.3847/1538-3881/aabc4f)

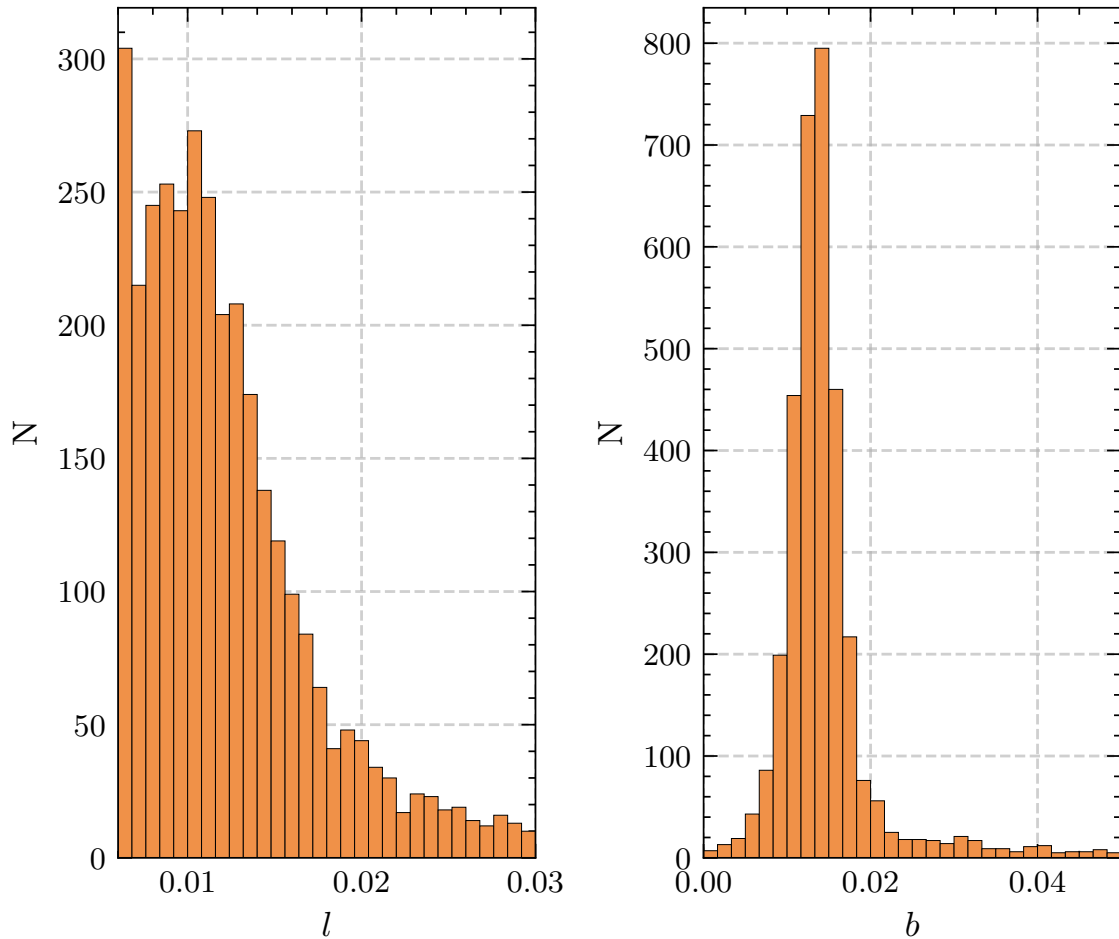


Figure 8. Distributions of the inferred hyperparameters for our CC sample. The panels show the distribution of posterior median values for l and b , respectively.

Astropy Collaboration, Price-Whelan, A. M., Lim, P. L., et al. 2022, *ApJ*, 935, 167, doi: [10.3847/1538-4357/ac7c74](https://doi.org/10.3847/1538-4357/ac7c74)

Bacon, R., Maineiri, V., Randich, S., et al. 2024, arXiv e-prints, arXiv:2405.12518, doi: [10.48550/arXiv.2405.12518](https://doi.org/10.48550/arXiv.2405.12518)

Belli, S., Newman, A. B., & Ellis, R. S. 2019, *ApJ*, 874, 17, doi: [10.3847/1538-4357/ab07af](https://doi.org/10.3847/1538-4357/ab07af)

Blake, C., & Glazebrook, K. 2003, *ApJ*, 594, 665, doi: [10.1086/376983](https://doi.org/10.1086/376983)

Borghini, N., Moresco, M., & Cimatti, A. 2022a, *ApJL*, 928, L4, doi: [10.3847/2041-8213/ac3fb2](https://doi.org/10.3847/2041-8213/ac3fb2)

Borghini, N., Moresco, M., Cimatti, A., et al. 2022b, *ApJ*, 927, 164, doi: [10.3847/1538-4357/ac3240](https://doi.org/10.3847/1538-4357/ac3240)

Brout, D., Scolnic, D., Popovic, B., et al. 2022, *ApJ*, 938, 110, doi: [10.3847/1538-4357/ac8e04](https://doi.org/10.3847/1538-4357/ac8e04)

Bruzual, G., & Charlot, S. 2003, *MNRAS*, 344, 1000, doi: [10.1046/j.1365-8711.2003.06897.x](https://doi.org/10.1046/j.1365-8711.2003.06897.x)

Buchner, J., Georgakakis, A., Nandra, K., et al. 2014, *A&A*, 564, A125, doi: [10.1051/0004-6361/201322971](https://doi.org/10.1051/0004-6361/201322971)

Calzetti, D., Armus, L., Bohlin, R. C., et al. 2000, *ApJ*, 533, 682, doi: [10.1086/308692](https://doi.org/10.1086/308692)

Carnall, A. C., McLure, R. J., Dunlop, J. S., & Davé, R. 2018, *MNRAS*, 480, 4379, doi: [10.1093/mnras/sty2169](https://doi.org/10.1093/mnras/sty2169)

Carnall, A. C., McLure, R. J., Dunlop, J. S., et al. 2019, *MNRAS*, 490, 417, doi: [10.1093/mnras/stz2544](https://doi.org/10.1093/mnras/stz2544)

Carnall, A. C., McLure, R. J., Dunlop, J. S., et al. 2022, *ApJ*, 929, 131, doi: [10.3847/1538-4357/ac5b62](https://doi.org/10.3847/1538-4357/ac5b62)

Charlot, S., & Longhetti, M. 2001, *MNRAS*, 323, 887, doi: [10.1046/j.1365-8711.2001.04260.x](https://doi.org/10.1046/j.1365-8711.2001.04260.x)

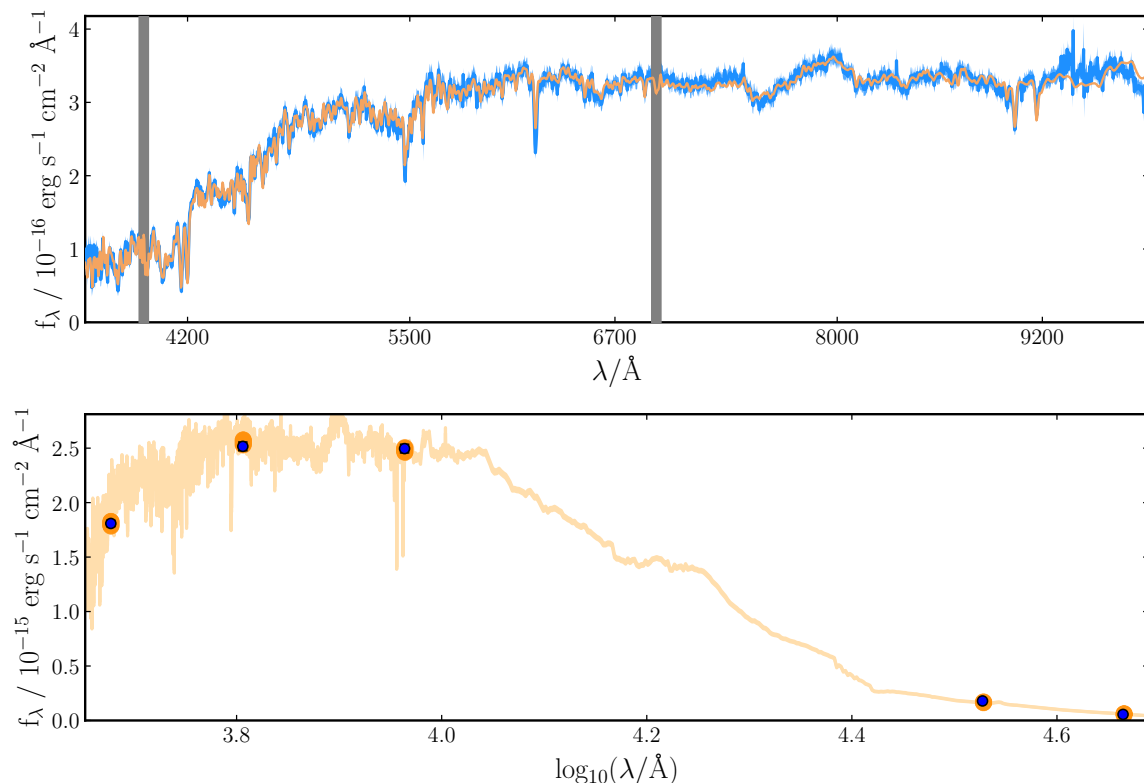


Figure 9. TARGETID = 2851244993413120 fitting result only with white noise.

- Cid Fernandes, R., Asari, N. V., Sodré, L., et al. 2007, *MNRAS*, 375, L16, doi: [10.1111/j.1745-3933.2006.00265.x](https://doi.org/10.1111/j.1745-3933.2006.00265.x)
- Cid Fernandes, R., Mateus, A., Sodré, L., Stasińska, G., & Gomes, J. M. 2005, *MNRAS*, 358, 363, doi: [10.1111/j.1365-2966.2005.08752.x](https://doi.org/10.1111/j.1365-2966.2005.08752.x)
- Citro, A., Pozzetti, L., Quai, S., et al. 2017, *MNRAS*, 469, 3108, doi: [10.1093/mnras/stx932](https://doi.org/10.1093/mnras/stx932)
- Conroy, C., Graves, G. J., & van Dokkum, P. G. 2014, *ApJ*, 780, 33, doi: [10.1088/0004-637X/780/1/33](https://doi.org/10.1088/0004-637X/780/1/33)
- Conroy, C., & Gunn, J. E. 2010, *ApJ*, 712, 833, doi: [10.1088/0004-637X/712/2/833](https://doi.org/10.1088/0004-637X/712/2/833)
- Conroy, C., Gunn, J. E., & White, M. 2009, *ApJ*, 699, 486, doi: [10.1088/0004-637X/699/1/486](https://doi.org/10.1088/0004-637X/699/1/486)
- Cowie, L. L., Songaila, A., Hu, E. M., & Cohen, J. G. 1996, *AJ*, 112, 839, doi: [10.1086/118058](https://doi.org/10.1086/118058)
- DESI Collaboration, Abdul-Karim, M., Adame, A. G., et al. 2025, arXiv e-prints, arXiv:2503.14745, doi: [10.48550/arXiv.2503.14745](https://doi.org/10.48550/arXiv.2503.14745)
- DESI Collaboration, Abareshi, B., Aguilar, J., et al. 2022, *AJ*, 164, 207, doi: [10.3847/1538-3881/ac882b](https://doi.org/10.3847/1538-3881/ac882b)
- Dey, A., Schlegel, D. J., Lang, D., et al. 2019, *AJ*, 157, 168, doi: [10.3847/1538-3881/ab089d](https://doi.org/10.3847/1538-3881/ab089d)
- Di Valentino, E., Mena, O., Pan, S., et al. 2021, *Classical and Quantum Gravity*, 38, 153001, doi: [10.1088/1361-6382/ac086d](https://doi.org/10.1088/1361-6382/ac086d)
- Eisenstein, D. 2003, arXiv e-prints, astro, doi: [10.48550/arXiv.astro-ph/0301623](https://doi.org/10.48550/arXiv.astro-ph/0301623)
- Eisenstein, D. J., Zehavi, I., Hogg, D. W., et al. 2005, *ApJ*, 633, 560, doi: [10.1086/466512](https://doi.org/10.1086/466512)
- Escamilla, L. A., Akarsu, Ö., Di Valentino, E., & Vazquez, J. A. 2023, *JCAP*, 2023, 051, doi: [10.1088/1475-7516/2023/11/051](https://doi.org/10.1088/1475-7516/2023/11/051)
- Ferland, G. J., Chatzikos, M., Guzmán, F., et al. 2017, *RMxAA*, 53, 385, doi: [10.48550/arXiv.1705.10877](https://doi.org/10.48550/arXiv.1705.10877)
- Feroz, F., Hobson, M. P., Cameron, E., & Pettitt, A. N. 2019, *The Open Journal of Astrophysics*, 2, 10, doi: [10.21105/astro.1306.2144](https://doi.org/10.21105/astro.1306.2144)
- Fitzpatrick, M. J., Olsen, K., Economou, F., et al. 2014, in *Society of Photo-Optical Instrumentation Engineers (SPIE) Conference Series*, Vol. 9149, *Observatory Operations: Strategies, Processes, and Systems V*, ed. A. B. Peck, C. R. Benn, & R. L. Seaman, 91491T, doi: [10.1117/12.2057445](https://doi.org/10.1117/12.2057445)

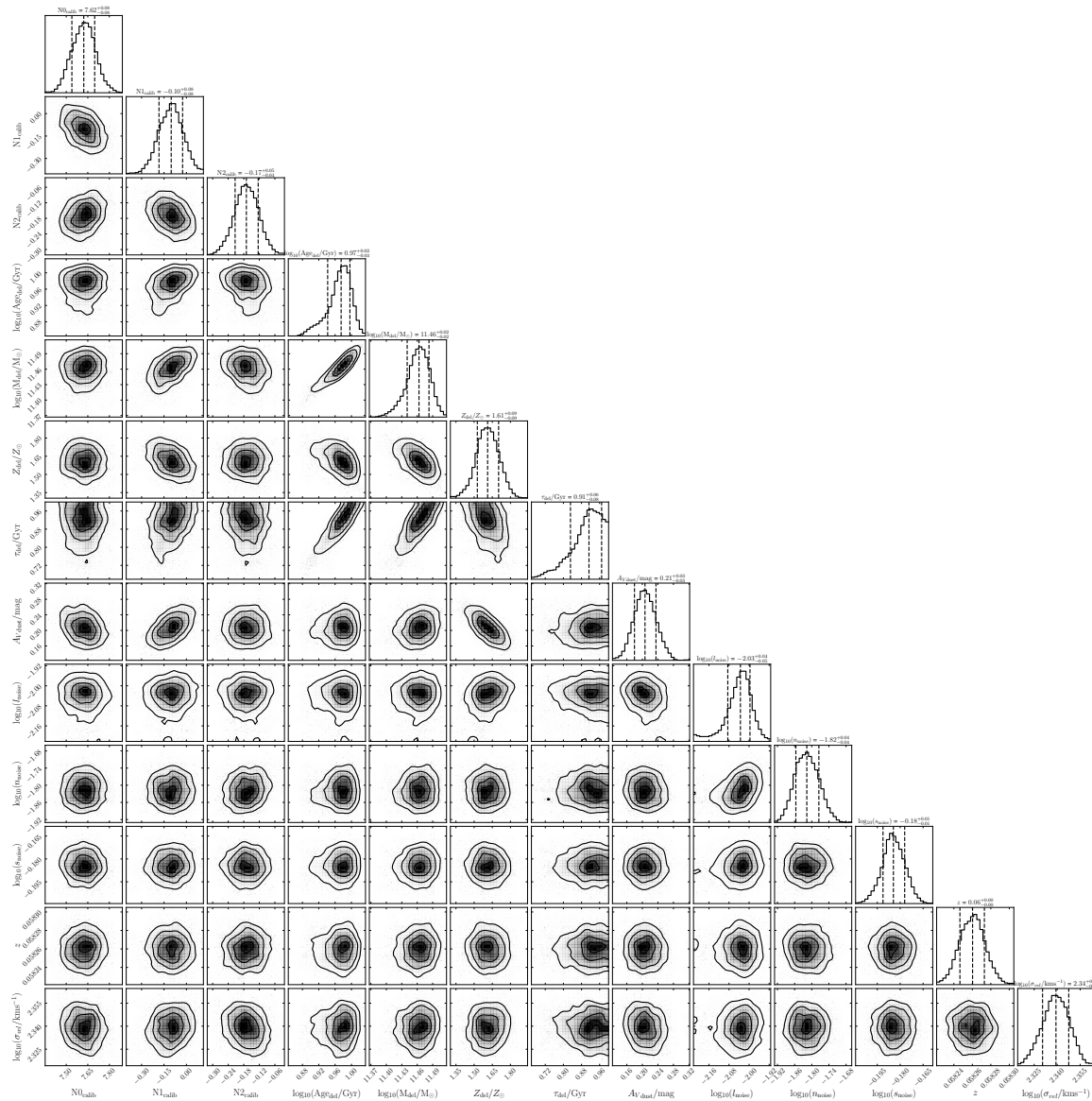


Figure 10. The posterior distribution corner plot of all fitted parameters (TARGETID = 2851244993413120).

Franx, M. 1995, in IAU Symposium, Vol. 164, Stellar Populations, ed. P. C. van der Kruit & G. Gilmore, 269

Gallazzi, A., Bell, E. F., Zibetti, S., Brinchmann, J., & Kelson, D. D. 2014, *ApJ*, 788, 72, doi: [10.1088/0004-637X/788/1/72](https://doi.org/10.1088/0004-637X/788/1/72)

Guy, J., Bailey, S., Kremin, A., et al. 2023, *AJ*, 165, 144, doi: [10.3847/1538-3881/acb212](https://doi.org/10.3847/1538-3881/acb212)

Harris, C. R., Millman, K. J., van der Walt, S. J., et al. 2020, *Nature*, 585, 357, doi: [10.1038/s41586-020-2649-2](https://doi.org/10.1038/s41586-020-2649-2)

Hartigan, J. A., & Hartigan, P. M. 1985, *The annals of Statistics*, 70

Hartigan, P. 1985, *Journal of the Royal Statistical Society. Series C (Applied Statistics)*, 34, 320

Herpich, F., Stasińska, G., Mateus, A., Vale Asari, N., & Cid Fernandes, R. 2018, *MNRAS*, 481, 1774, doi: [10.1093/mnras/sty2391](https://doi.org/10.1093/mnras/sty2391)

Hubble, E. P. 1982, *The realm of the nebulae*, Vol. 25 (Yale University Press)

Ilbert, O., McCracken, H. J., Le Fèvre, O., et al. 2013, *A&A*, 556, A55, doi: [10.1051/0004-6361/201321100](https://doi.org/10.1051/0004-6361/201321100)

Jiao, K., Borghi, N., Moresco, M., & Zhang, T.-J. 2023, *ApJS*, 265, 48, doi: [10.3847/1538-4365/acbc77](https://doi.org/10.3847/1538-4365/acbc77)

- Jimenez, R., & Loeb, A. 2002, *ApJ*, 573, 37,
doi: [10.1086/340549](https://doi.org/10.1086/340549)
- Jimenez, R., Moresco, M., Verde, L., & Wandelt,
B. D. 2023, *JCAP*, 2023, 047,
doi: [10.1088/1475-7516/2023/11/047](https://doi.org/10.1088/1475-7516/2023/11/047)
- Kamionkowski, M., & Riess, A. G. 2023, *Annual
Review of Nuclear and Particle Science*, 73, 153,
doi: [10.1146/annurev-nucl-111422-024107](https://doi.org/10.1146/annurev-nucl-111422-024107)
- Kriek, M., Price, S. H., Conroy, C., et al. 2019,
ApJL, 880, L31, doi: [10.3847/2041-8213/ab2e75](https://doi.org/10.3847/2041-8213/ab2e75)
- Kroupa, P. 2001, *MNRAS*, 322, 231,
doi: [10.1046/j.1365-8711.2001.04022.x](https://doi.org/10.1046/j.1365-8711.2001.04022.x)
- Lange, J. U. 2023, *MNRAS*, 525, 3181,
doi: [10.1093/mnras/stad2441](https://doi.org/10.1093/mnras/stad2441)
- Laureijs, R., Amiaux, J., Arduini, S., et al. 2011,
arXiv e-prints, arXiv:1110.3193,
doi: [10.48550/arXiv.1110.3193](https://doi.org/10.48550/arXiv.1110.3193)
- Lei, L., Wang, Z.-F., Wang, T.-L., et al. 2026,
MNRAS, 547, stag430,
doi: [10.1093/mnras/stag430](https://doi.org/10.1093/mnras/stag430)
- Leung, H.-H., Wild, V., Papatthomas, M., et al.
2024, *MNRAS*, 528, 4029,
doi: [10.1093/mnras/stae225](https://doi.org/10.1093/mnras/stae225)
- Loubser, S. I., Alabi, A. B., Hilton, M., et al. 2025,
MNRAS, 540, 3135, doi: [10.1093/mnras/staf915](https://doi.org/10.1093/mnras/staf915)
- Miller, T. N., Doel, P., Gutierrez, G., et al. 2024,
AJ, 168, 95, doi: [10.3847/1538-3881/ad45fe](https://doi.org/10.3847/1538-3881/ad45fe)
- Moresco, M. 2015, *MNRAS*, 450, L16,
doi: [10.1093/mnrasl/slv037](https://doi.org/10.1093/mnrasl/slv037)
- Moresco, M., Jimenez, R., Cimatti, A., &
Pozzetti, L. 2011, *JCAP*, 2011, 045,
doi: [10.1088/1475-7516/2011/03/045](https://doi.org/10.1088/1475-7516/2011/03/045)
- Moresco, M., Jimenez, R., Verde, L., et al. 2018,
ApJ, 868, 84, doi: [10.3847/1538-4357/aae829](https://doi.org/10.3847/1538-4357/aae829)
- Moresco, M., Cimatti, A., Jimenez, R., et al. 2012,
JCAP, 2012, 006,
doi: [10.1088/1475-7516/2012/08/006](https://doi.org/10.1088/1475-7516/2012/08/006)
- Moresco, M., Pozzetti, L., Cimatti, A., et al. 2013,
A&A, 558, A61,
doi: [10.1051/0004-6361/201321797](https://doi.org/10.1051/0004-6361/201321797)
- Moresco, M., Pozzetti, L., Cimatti, A., et al. 2016,
JCAP, 2016, 014,
doi: [10.1088/1475-7516/2016/05/014](https://doi.org/10.1088/1475-7516/2016/05/014)
- Moresco, M., Amati, L., Amendola, L., et al. 2022,
Living Reviews in Relativity, 25, 6,
doi: [10.1007/s41114-022-00040-z](https://doi.org/10.1007/s41114-022-00040-z)
- Nikutta, R., Fitzpatrick, M., Scott, A., & Weaver,
B. A. 2020, *Astronomy and Computing*, 33,
100411, doi: [10.1016/j.ascom.2020.100411](https://doi.org/10.1016/j.ascom.2020.100411)
- Noll, S., Burgarella, D., Giovannoli, E., et al.
2009, *A&A*, 507, 1793,
doi: [10.1051/0004-6361/200912497](https://doi.org/10.1051/0004-6361/200912497)
- Onodera, M., Renzini, A., Carollo, M., et al. 2012,
ApJ, 755, 26, doi: [10.1088/0004-637X/755/1/26](https://doi.org/10.1088/0004-637X/755/1/26)
- Panther, B., Heavens, A. F., & Jimenez, R. 2003,
MNRAS, 343, 1145,
doi: [10.1046/j.1365-8711.2003.06722.x](https://doi.org/10.1046/j.1365-8711.2003.06722.x)
- Percival, W. J., Baugh, C. M., Bland-Hawthorn,
J., et al. 2001, *MNRAS*, 327, 1297,
doi: [10.1046/j.1365-8711.2001.04827.x](https://doi.org/10.1046/j.1365-8711.2001.04827.x)
- Planck Collaboration, Aghanim, N., Akrami, Y.,
et al. 2020, *A&A*, 641, A6,
doi: [10.1051/0004-6361/201833910](https://doi.org/10.1051/0004-6361/201833910)
- Poppett, C., Tyas, L., Aguilar, J., et al. 2024, *AJ*,
168, 245, doi: [10.3847/1538-3881/ad76a4](https://doi.org/10.3847/1538-3881/ad76a4)
- Pozzetti, L., Bolzonella, M., Zucca, E., et al. 2010,
A&A, 523, A13,
doi: [10.1051/0004-6361/200913020](https://doi.org/10.1051/0004-6361/200913020)
- Ratsimbazafy, A. L., Loubser, S. I., Crawford,
S. M., et al. 2017, *MNRAS*, 467, 3239,
doi: [10.1093/mnras/stx301](https://doi.org/10.1093/mnras/stx301)
- Riess, A. G., Filippenko, A. V., Challis, P., et al.
1998, *AJ*, 116, 1009, doi: [10.1086/300499](https://doi.org/10.1086/300499)
- Schlafly, E. F., Kirkby, D., Schlegel, D. J., et al.
2023, *AJ*, 166, 259,
doi: [10.3847/1538-3881/ad0832](https://doi.org/10.3847/1538-3881/ad0832)
- Serra, P., Amblard, A., Temi, P., et al. 2011, *ApJ*,
740, 22, doi: [10.1088/0004-637X/740/1/22](https://doi.org/10.1088/0004-637X/740/1/22)
- Silber, J. H., Fagrelus, P., Fanning, K., et al.
2023, *AJ*, 165, 9, doi: [10.3847/1538-3881/ac9ab1](https://doi.org/10.3847/1538-3881/ac9ab1)
- Simon, J., Verde, L., & Jimenez, R. 2005, *PhRvD*,
71, 123001, doi: [10.1103/PhysRevD.71.123001](https://doi.org/10.1103/PhysRevD.71.123001)
- Singh, R., van de Ven, G., Jahnke, K., et al. 2013,
A&A, 558, A43,
doi: [10.1051/0004-6361/201322062](https://doi.org/10.1051/0004-6361/201322062)
- Smoot, G. F., Bennett, C. L., Kogut, A., et al.
1992, *ApJL*, 396, L1, doi: [10.1086/186504](https://doi.org/10.1086/186504)
- Stern, D., Jimenez, R., Verde, L., Kamionkowski,
M., & Stanford, S. A. 2010, *JCAP*, 2010, 008,
doi: [10.1088/1475-7516/2010/02/008](https://doi.org/10.1088/1475-7516/2010/02/008)
- Thomas, D., Maraston, C., Schawinski, K., Sarzi,
M., & Silk, J. 2010, *MNRAS*, 404, 1775,
doi: [10.1111/j.1365-2966.2010.16427.x](https://doi.org/10.1111/j.1365-2966.2010.16427.x)
- Tomasetti, E., Moresco, M., Borghi, N., et al.
2023, *A&A*, 679, A96,
doi: [10.1051/0004-6361/202346992](https://doi.org/10.1051/0004-6361/202346992)
- Tomasetti, E., Moresco, M., Borghi, N., et al.
2025, *arXiv e-prints*, arXiv:2512.22964,
doi: [10.48550/arXiv.2512.22964](https://doi.org/10.48550/arXiv.2512.22964)

- Vagnozzi, S., Pacucci, F., & Loeb, A. 2022, *Journal of High Energy Astrophysics*, 36, 27, doi: [10.1016/j.jheap.2022.07.004](https://doi.org/10.1016/j.jheap.2022.07.004)
- van Dokkum, P. G., Franx, M., Fabricant, D., Illingworth, G. D., & Kelson, D. D. 2000, *ApJ*, 541, 95, doi: [10.1086/309402](https://doi.org/10.1086/309402)
- Virtanen, P., Gommers, R., Oliphant, T. E., et al. 2020, *Nature Methods*, 17, 261, doi: [10.1038/s41592-019-0686-2](https://doi.org/10.1038/s41592-019-0686-2)
- Wang, Y.-Y., Lei, L., Tang, S.-P., & Fan, Y.-Z. 2026, *JCAP*, 2026, 009, doi: [10.1088/1475-7516/2026/01/009](https://doi.org/10.1088/1475-7516/2026/01/009)
- Wes McKinney. 2010, in *Proceedings of the 9th Python in Science Conference*, ed. Stéfan van der Walt & Jarrod Millman, 56 – 61, doi: [10.25080/Majora-92bf1922-00a](https://doi.org/10.25080/Majora-92bf1922-00a)
- Zhang, C., Zhang, H., Yuan, S., et al. 2014, *Research in Astronomy and Astrophysics*, 14, 1221, doi: [10.1088/1674-4527/14/10/002](https://doi.org/10.1088/1674-4527/14/10/002)
- Zou, H., Zhou, X., Fan, X., et al. 2017, *PASP*, 129, 064101, doi: [10.1088/1538-3873/aa65ba](https://doi.org/10.1088/1538-3873/aa65ba)
- Zou, H., Sui, J., Saintonge, A., et al. 2024, *ApJ*, 961, 173, doi: [10.3847/1538-4357/ad1409](https://doi.org/10.3847/1538-4357/ad1409)